

See discussions, stats, and author profiles for this publication at: <https://www.researchgate.net/publication/230746550>

Microtomographic Quantification of Hydraulic Clay Mineral Displacement Effects During a CO₂ Sequestration Experiment with Saline Aquifer Sandstone

ARTICLE *in* ENVIRONMENTAL SCIENCE & TECHNOLOGY · AUGUST 2012

Impact Factor: 5.33 · DOI: 10.1021/es3013358 · Source: PubMed

CITATIONS

9

READS

55

4 AUTHORS, INCLUDING:



Kathleen Sell

Johannes Gutenberg-Universität Mainz

10 PUBLICATIONS 13 CITATIONS

SEE PROFILE



Frieder Enzmann

Johannes Gutenberg-Universität Mainz

63 PUBLICATIONS 489 CITATIONS

SEE PROFILE



Michael Kersten

Johannes Gutenberg-Universität Mainz

137 PUBLICATIONS 2,131 CITATIONS

SEE PROFILE

Microtomographic Quantification of Hydraulic Clay Mineral Displacement Effects During a CO₂ Sequestration Experiment with Saline Aquifer Sandstone

Kathleen Sell,[†] Frieder Enzmann,[†] Michael Kersten,^{†,*} and Erik Spangenberg[‡]

[†]Geosciences Institute, Johannes Gutenberg University, Mainz 55099, Germany

[‡]Helmholtz Centre GFZ Potsdam, Reservoir Technologies Section, Telegrafenberg E223, Potsdam 14473, Germany

S Supporting Information

ABSTRACT: We combined a noninvasive tomographic imaging technique with an invasive open-system core-flooding experiment and compared the results of the pre- and postflooded states of an experimental sandstone core sample from an ongoing field trial for carbon dioxide geosequestration. For the experiment, a rock core sample of 80 mL volume was taken from the 629 m Stuttgart Formation storage domain of a saline sandstone aquifer at the CCS research pilot plant Ketzin, Germany. Supercritical carbon dioxide and synthetic brine were injected under in situ reservoir p/T-conditions at an average flow rate of 0.1 mL/min for 256 h. X-ray computed microtomographic imaging was carried out before and after the core-flooding experiment at a spatial voxel resolution of 27 μm . No significant changes in microstructure were found at the tomographic imaging resolution including porosity and pore size distribution, except of an increase of depositional heterogeneous distribution of clay minerals in the pores. The digitized rock data were used as direct real microstructure input to the GeoDict software package, to simulate Navier–Stokes flow by a lattice Boltzmann equation solver. This procedure yielded 3D pressure and flow velocity fields, and revealed that the migration of clay particles decreased the permeability tensor probably due to clogging of pore openings.



INTRODUCTION

Effective targeting of research efforts to reduce industrial carbon dioxide (CO₂) emissions by geosequestration, while preserving access to fossil fuel energy resources, requires quantitative methods to understand subsurface fluid behavior of the storing CO₂. Saline aquifers in sandstone host rocks are advocated as a potential carbon capture and storage (CCS) option alternative to already existing hydrocarbon extraction sites when considering injectivity, vertical permeability, reservoir hydrodynamics, geochemical interactions and long-term containment.¹ This is because, unlike carbonaceous formations, siliciclastic sedimentary rocks chosen for residual trapping are not expected to develop deleterious geochemical reactions with the supercritical CO₂ (scCO₂) injectate. A promising natural saline sandstone aquifer is located in Ketzin near Berlin, NE Germany. It hosts the CCS pilot plant "CO₂SINK" (www.co2sink.org) which was found adequate for geosequestration in terms of structural geology,² petrology,³ and hydro-geochemistry.⁴ This site is not linked to hydrocarbon operations, as is often the case with geosequestration options, but there are a number of major coal power plants in the vicinity. Since the start of injection in June 2008 up to February 2012, more than 58 000 tons of CO₂ have been injected and stored in the saline aquifer. From a hydrogeological point of view, this aquifer meets the requirements for a suitable CO₂ geosequestration reservoir, in that no essential consequences for the integrity of the rocks have been found due to the interactions with the fluids. The high salinity of the aquifer brine is favored due to its role in secondary mineral

formation, the so-called "mineral trapping option". However, the use of this option is expected to induce changes in permeability, albeit at a rate and degree that cannot be predicted accurately due to a paucity of experimental data on 4D permeability anisotropy, and factors that affect them. Colloidal particle remobilization on a subcore scale, which has for some time been expected to induce changes in permeability as well, has to our knowledge been quantified for caprocks but not in the storage domain.^{5,6} Ultimately, computational simulations were not sufficiently capable of describing the real temporal and spatial distribution of the CO₂ at the Ketzin site which warrants a more detailed research in underground permeability development.⁷

Our investigations comprised a core-flooding experiment to investigate the effects of permeability changes in rock samples from this site. The goal of the study was to perform computed microtomography scans of sandstone plugs before and after scCO₂ treatment at in situ reservoir conditions to visualize, quantify and model (i) any alterations expected in the real microstructure, in particular, any flushing/flotation and redistribution of fine-grained material mobilized within the pore space, and (ii) any gradual changes in the hydrodynamic

Special Issue: Carbon Sequestration

Received: April 20, 2012

Revised: August 22, 2012

Accepted: August 27, 2012

parameters, such as the permeability tensor, that these alterations might induce.

MATERIALS AND METHODS

Materials. The sandstone core subsample B2–3a was taken from the Triassic Stuttgart Formation at Ketzin, Germany.⁴ This lithographic formation is characterized by muddy flood plain facies of poor reservoir quality alternating with sandstone channels of high reservoir quality.⁸ The saline aquifer is part of a large channel-string system that is 8 km wide and 30 m thick, and located at a depth of ≥ 620 m in the central and western part of the Roskow-Ketzin double anticline.⁹ The sandstone is of an Arkose-type with a mineral composition that X-ray diffraction analysis showed as being dominated by, on average, 50 wt.-% feldspar (albite, analcime, microcline, orthoclase) and 38 wt.-% quartz, with an elevated low-iron clay mineral content (9 wt.-% chlorite and Illite), and minor amounts of Fe-bearing minerals (3 wt.-% hematite and maghemite) but no traceable carbonates (<0.1 wt.-%, unpublished data, CO2SINK project data archive). Scanning electron microscope images show that the clay minerals fill up the pore spaces.¹⁰ Hydraulic well tests revealed a good permeability of 500–1000 mD (1 mD = 10^{-9} m²).¹¹ The rock core sample was stored in brine obtained from the Ketzin site to prevent drying and hence salt precipitation in the pore space.¹² However, the natural brine with total dissolved solids of up to about 244 g L⁻¹ was not used for the flooding experiment. Instead, synthetic brine representing major components of the reservoir brine listed in Table 1 with

Table 1. Composition of the Synthetical Brine Used for the Core-Flooding Experiment^a

salt	amount (g/L)	(wt.-%)
MgSO ₄	4.0	1.6
Na ₂ SO ₄	1.3	0.5
CaCl ₂	6.4	2.6
KCl	0.7	0.3
NaCl	215	88.3
MgSO ₄ ·7H ₂ O	8.0	3.3
CaCl ₂ ·2H ₂ O	8.4	3.4
TDS	244	100

^aTDS denotes total dissolved solids.

same total dissolved solids was used. Currently, there is no known possibility of capturing pure CO₂ after fossil burning processes. In light of this practical limit, in our investigations carbon dioxide with an impurity of 3% oxygen was used as a feasible optimum in terms of loss of storage capacity and consumption of energy during CO₂ separation.

Experimental Core-Flooding Setup. As an optimum trade-off between the requirements of tomography with respect to resolution and energy spectrum on the one hand and material stability during the high-pressure flooding experiment on the other, a sample size with a diameter of 47.6 mm but a length of only 46.0 mm (81.8 cm³) was used. The combination of a saline brine, scCO₂, and oxygen is a strong corrosive agent, so it was essential that steps be taken to avoid the gas-brine-mixture coming into contact with any corrodible material. To this end, the plug was covered at its ends with stainless-steel caps and jacketed in a heat-shrinkable sleeve. The caps contained fluid ports made of polytetrafluoroethylene (PTFE). To enable a better distribution of fluid, the cap's surface was grooved on the injection side.

The sandstone plug was treated in the “Field Laboratory Experimental Core Analyses System” (FLECAS) at the Helmholtz Centre GFZ Potsdam, Germany, as described in detail previously.¹³ In brief, the rig consists of a steel autoclave cell filled with hydraulic oil wherein the jacketed sample is placed. Four syringe pumps (Teledyne ISCO 500D) provide the internal pressure flow. One of the pumps is filled with the artificial brine and one with the gas mixture. The experimental setup is an open system in which the third pump receives the gas-brine mix after the core has been flooded. The fourth pump controls the hydrostatic confining pressure of 15 MPa. The rate of injection of the pore fluid keeps its pressure constant at a lower value of 7.5 MPa. The equipment also includes electrical heating, which is used to maintain a constant in situ reservoir temperature of 40 °C. The applied p/T-conditions also ensured that the CO₂ was kept in a supercritical state to avoid known adverse effects that are due to separation of scCO₂ into liquid and gas phases, as has been reported occasionally for experiments with carbonate reservoir rocks.¹⁴

Initially, the synthetic brine was injected to the sample at a constant flow rate of 0.1 mL min⁻¹ through the bottom fluid port on the sample. Rates of injection flow were monitored directly by the software that controls the syringe pumps. After approximately four pore volumes (PV) of brine had been injected, steady state was achieved.

Subsequently, the fractional flow of the scCO₂ was increased during the next 6 PV until the fluid became almost brine-free (100% scCO₂ flow). The procedure was chosen to simulate a slow increase in the amount of scCO₂ within the saline aquifer. Ultrasonic measurements were taken at a resonance frequency of 500 kHz by piezoelectric transducers that were placed in the end-caps to monitor the poroelastic wave propagation. The value of V_p/V_s decreased as the fractional scCO₂ flow increased, which ensure that no mechanical cracking of the sample occurred during the high-pressure experiment.

The plug was further flushed for 9 days at a constant rate with 100% scCO₂. Then, the fractional scCO₂ flow was reversed for the injection of the next 6 PV. As a result, pure brine flow was achieved again, which mimicked the initial conditions of the sample, thereby enabling an accurate comparison of the microstructures before and after scCO₂ treatment. The experiment lasted for a total of 256 h, during which time 1.5 L of fluid was forced through the plug (≈ 150 PV at an initial open porosity of 12%).

Tomography Experiment. High-resolution X-ray computed microtomography (μ -XCT) was conducted at the facilities of the Federal Institute for Material Research and Testing in Berlin, Germany. The sandstone plug was scanned under the same experimental μ -XCT conditions before and after being treated with scCO₂. The CT facility consists of a 225 kV microfocus X-ray tube with a Perkin-Elmer 1620 a.m.3 flat panel detector and a CsI scintillator screen that includes 2048 × 2048 elements, each 200 × 200 μ m². The beam parameters used during the measurements were 190 kV and 75 μ A. The angle viewing step size was set to 0.2 degrees, which yielded a total of 1800 slice projections over 360°, with an integration time of 20 s per projection. The 3D data set was reconstructed to an image matrix of 1993 × 1993 × 1785 voxels, with a voxel size of 27.1 μ m resulting from the selected magnification. Image artifacts, such as beam hardening, have a strong effect on the quality of the scan's resolution and might affect the correctness of the segmentation process. To avoid

these artifacts, the beam was prefiltered using a 0.5 mm silver foil.

Every gray scale image derived from computed tomography contains noise that must be reduced to provide a good quality of segmentation. For this purpose, an anisotropic digital median filter was used, calibrated for the appropriate dimensions and kernel window sizes.¹⁵ The replacement of voxels using the approximated median of neighboring voxels causes smoothing of the raw data. Six different regions of interest (ROIs), each of $512 \times 512 \times 512$ voxels, were chosen from the original data set by using the AMIRA visualization software tool (locations shown in Figure S1 of Supporting Information (SI)). These ROIs, which were located at the same places before and after the core was flooded, were then segmented to classify features of particular interest, such as phase distributions in the μ -XCT files.^{16–19} The steps of the segmentation process are shown in Figure S2 (SI) and include the transformation of voxels comprising a gray scale range (GSR) by global thresholding into four classes: pores (GSR = 1–9280), quartz and feldspar matrix (GSR = 9281–10 446), clay minerals (GSR = 10 447–12 480), and iron-rich minerals (GSR = 12 481–60 000). These thresholds were chosen to reproduce the mineral composition known from the X-ray diffraction and thin section analysis in the petrologic microscope. The segmentation was exactly the same for both the pre- and postflooding core images, which meant that any absolute error introduced by the segmentation was the same for both states, so only the relative deviations were of interest. An assessment of the relative error introduced by slight shifts in the thresholding between both states is given in the SI.

A 3D volume rendering was ultimately performed to visualize the 2D slices as a stacked 3D volume data set.²⁰ Changes in the μ -XCT data before and after treatment were interpreted using the GeoDict (Geometric Models and Predictions of Properties) software package developed by Fraunhofer ITWM and distributed by Math2Market GmbH, Kaiserslautern, Germany (<http://www.geodict.com>). Screenshots of this industrial simulation software are provided in the SI. The authors collaborated with the developers of the software to adapt it so that it could quantify the changes in tomography data of geologic media in terms of the actual porosity and permeability of the pore space and migration of clay minerals. To estimate the pore space parameters, a bin size was chosen that agreed with the effective voxel resolution of $27.1 \mu\text{m}$. Therefore, all voxels of the sampled ROI (a total of 1.34×10^8 each) were considered for a GeoDict simulation run to obtain acceptable statistical results. A common albeit somewhat arbitrary criterion required to partition pore space into individual pores with a characteristic pore-size distribution is identification in 3D of pore bodies in between narrower pore openings (or capillary constrictions). The PoroDict module of the software package provides information on both the geometric pore size distribution (PSD) based on delineation of the thus characterized pore bodies, but also by the results of a simulation of a mercury intrusion porosimetry (MIP) experiment the effective capillary size distribution. The main principle of the estimation of the geometric PSD is to fit virtual spheres into the pore volumes, the “maximum inscribed spheres” (MIS) approach. While this purely geometrical MIS-PSD approach takes both connected and disconnected pores into account, the MIP-PSD simulation yields results only on connected pores. Connected and disconnected pores (open/closed porosity) may thus be distinguished as well.^{21–23} For every range of pore

size in the MIP-PSD approach, a specific surface tension needs to be simulated to force the virtual mercury into the pore. In addition, the contact angle of the virtual mercury fluid is fixed during the simulation runs and can be set according to the liquid surface tension.²³ All microstructure parameters that were thus derived were calculated as mean and standard deviation from the 5–6 different ROIs selected (Tables 2 and 3).

Table 2. Comparison of the Total Porosity (ϕ) and Closed Porosity (ϕ_c) in Different ROIs of the Pre- And Post-Flooded Sample State, Where the Latter Is Denoted with an Asterisk^a

ROI no.	ϕ	ϕ^*	ϕ_c	ϕ_c^*	ϕ_o	ϕ_o^*
1	7.5	7.2	3.2	3.4	4.3	3.8
2	18.5	17.2	0.8	1.0	17.7	16.2
3	16.5	14.9	1.4	1.5	15.1	13.4
4	16.1	14.4	1.7	1.7	14.4	12.7
5	16.5	14.7	1.9	2.2	14.6	12.5
6	14.1	13.9	1.6	1.9	12.5	12.0
mean 2–6	16.5	15.1	1.6	1.8	15.0	13.5
SD	1.4	1.2	0.3	0.4	1.7	1.6

^aThe difference between these two porosities is the open (connected) porosity (ϕ_o , ϕ_o^*) used in further calculations.

Table 3. Geometric Pore Size Distribution (MIS-PSD in μm) and Virtual Mercury Intrusion Simulation (MIP-PSD) Carried out with GeoDict for the Four Different ROIs^a

ROI no.	D10		D10*	
	MIS-PSD	MIP-PSD	MIS-PSD	MIP-PSD
1	30.9	5.4	30.9	4.8
2	32.0	28.4	32.2	28.4
3	31.8	28.1	32.0	25.4
4	35.2	22.7	35.8	22.5
5	34.7	27.8	34.8	24.7
6	35.0	23.6	35.7	23.6
mean 2–6	32.9	22.5	33.1	24.9
SD	1.7	2.4	1.8	2.0
		D50	D50*	
1	46.0	27.2	46.1	24.2
2	51.7	41.7	52.6	41.7
3	50.8	40.2	51.6	40.9
4	57.2	42.2	58.0	45.1
5	61.1	40.8	60.8	43.5
6	57.3	42.5	57.3	44.1
mean 2–6	55.6	41.5	56.1	43.1
SD	3.8	0.9	3.5	1.5
		D90	D90*	
1	79.0	49.2	79.1	48.5
2	96.4	60.0	96.4	60.0
3	95.2	52.2	101.1	58.5
4	101.5	62.3	99.9	68.5
5	104.0	59.6	104.7	61.2
6	103.7	61.9	106.3	62.8
mean 2–6	100.2	59.2	101.7	62.2
SD	3.7	3.7	3.5	3.4

^aThe percentiles D10, D50, and D90 of the pore diameter in μm are shown for the pre- and post-flooded (D, D*) states, indicating no significant change.

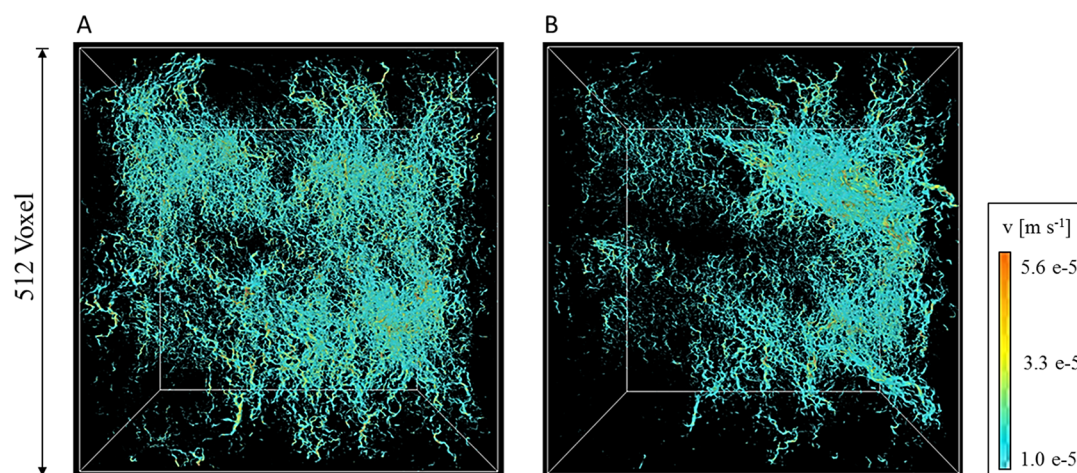


Figure 1. The modeled velocity field in the z -direction, shown for the preflooded (A) and postflooded state (B) of ROI no. 3.

RESULTS AND DISCUSSION

Comparison of Pre- and Postflooding Status by μ -XCT Visualization. The majority of the pores ($>80\%$) were found to be connected (open porosity). However, any quantification of pore space parameters is hampered by the heterogeneity of the sample, in that in some parts of the sample the number of pores increases while in others it decreases. Averages of the total porosities of the treated and the nontreated sample states for six different ROIs are listed in Table 2. ROI No. 1 was not chosen for the calculation of the mean and standard deviation because it lies in a clay-bearing region with a total porosity of only 7.5%, so it is thus not representative of the main scCO_2 pathways. This heterogeneity of the pore space is in a range typical for Arkose sandstone.²⁴ The difference in the mean open porosity for the other five ROIs was $15.0 \pm 1.7\%$ before and $13.5 \pm 1.6\%$ after flooding which is not significant due to the heterogeneity of the sample (Table 2). Table 3 presents a summary of all computed PSD parameters, which also shows insignificant pre- and postflood differences in the same median pore diameter ranges of D10, D50, and D90 for (respectively) the 10%, 50%, and 90% fractions of the cumulative pore size in the five different ROIs. The difference in results between the MIS-PSD and the MIP-PSD simulation approach increases with the fraction of the cumulative pore size which suggests a better connectivity of the smaller pores.

Fluid Flow Simulation at the Pore-Scale. Permeability can, in principle, be estimated by using the digitized rock data directly to simulate Newtonian fluid flow through the segmented pore space of the sample.^{25–30} The flow simulation was based on solving the discrete lattice Boltzmann equation (LBE) model on a regular cubic lattice derived from μ -XCT for a numerical grid generation. One cubic voxel of the CT image equals a unit cell of the LBE grid. A 15-vector of velocity space is represented by the implementation of the D3Q15 mode of the LBM with a multiple relaxation time (MRT) approximation. The major advantage of the MRT-LBE approach over the classical Bhatnagar–Gross–Krook approach is its improved numerical stability.^{30,31} The GeoDict software includes also a MRT-LBE simulation module for multiphase flow.³² However, in this preliminary modeling approach only single-phase flow of the brine was modeled for the determination of hydrodynamic changes in the saline aquifer, before and after, but not during, scCO_2 treatment.

The pressure gradient and velocity tensor were chosen as the outputs of the simulations, which were performed in a space of 1.34×10^8 voxels on a HPC comprising four Interlagos processors, each of them including 12 cores, and a total RAM capacity of 512 GB. Less than 1 day of CPU time was necessary per simulation run on this desktop HPC. The boundary conditions were set to a periodic state and were obtained for all computational directions, implying that media passing over one boundary will subsequently appear on the opposite site, following the same direction of flow. The input required for the LBE solver to achieve a Navier–Stokes (flow) solution was modified to calculate the fluid velocity field by specifying a brine density of $\rho = 1.165 \text{ g cm}^{-3}$ and a viscous friction with a dynamic viscosity $\mu = 6.75 \times 10^{-4} \text{ Pa}\cdot\text{s}$ at a reservoir temperature of $T = 40^\circ\text{C}$. The flow permeability coefficient k thus computed refers to a steady-state Newtonian fluid flow defined by its dynamic viscosity under isothermal conditions. The accuracy in the permeability for which steady state was achieved at 10 000 iteration steps is in the order of 5×10^{-4} (see SI). The flow simulations were performed in all three Cartesian x -, y -, and z -directions. A constant pressure drop of 1 Pa over the distance between opposite edges along those directions was applied for full saturation of the pore space. The computed velocity vector field and pressure gradient in each of those directions were used to calculate the permeability tensor. In a 3D Cartesian coordinate system, this tensor is an important hydrodynamic parameter for describing the hydrodynamic behavior of an anisotropic pore medium.

Figure 1 shows, as an example, the velocity field only in the z -direction, which represents the direction of core-flooding. The fluid velocity ranged from very low to high, as expected for an heterogeneous porous medium, but the major velocities ranged between low and moderate, with low shown as blue, and moderate as turquoise in Figure 1. The two main (bluish-turquoise) velocity flow fields are separated by the effects of a less permeable clay-rich layer. Because the flow was forced by a pressure gradient, applied along the z -direction in Figure 1, the mean flow field established along the less permeable clay layers became stratified almost perpendicular to the pressure gradient. While the permeability modeled in z -direction agrees with that measured in field, the pore connectivity and thus permeability in the x - and y -directions is clearly better. Another main result yielded by calculating the permeability tensor is the significant change after the core was flooded by scCO_2 . Surprisingly, for all

ROIs and directions calculated, the permeability, but not the porosity or distribution of pores according to size, was found to be lower after scCO₂ treatment. Although all 15 individual numbers were thus lower, the difference in the means is not significant due to the large heterogeneity (Table 4). No change

Table 4. Permeability Tensor of the Three Main Directories for Different ROIs of the Pre- And Post-Flooded Sample State, Where the Latter Is Denoted with an Asterisk^a

ROI #	x-direction	y-direction	z-direction
2	2813	3182	1003
3	1847	2979	522
4	2413	2580	971
5	1127	1409	572
6	2275	2095	702
mean	2252	2616	806
SD	505	574	197
2*	2344	2594	888
3*	1660	1783	335
4*	1870	2559	893
5*	1028	1021	322
6*	1792	1846	530
mean	1842	2133	702
SD	391	520	240

^aThe unit is mD (1 mD = 10^{−9} m²).

was found in the total clay mineral (voxel = volumetric) abundance in ROIs 2–6 before (24.0 ± 2.5%) and after (24.0 ± 2.6%) core-flooding, while μ -XCT revealed rearrangement of clay mineral assemblages in shape and size in the sample (Figure 2).

Therefore, a possible explanation for the change in permeability is that pore openings are clogged by the migration of these particles due to a flotation effect by the scCO₂ fluid, rather than the brine simply flushing them out. On the other hand, the possibility cannot be ruled out that the pore openings were clogged by precipitates smaller than the voxel resolution of 27 μ m.

Implications of the μ -XCT Results. The injection of scCO₂ was expected to result in a variety of strongly interlinked physical and chemical processes, including multiphase flow,

dissolution–precipitation kinetics, solute transport, hydrodynamic instabilities, and viscous capillary effects, such as fingering caused by contrasts in viscosity between scCO₂ and brine.^{6,14,33} In previous studies, changes in porosity were measured on the basis of changes in the mass of the solid plugs, or in the balances of dissolved components, the latter down to the order of 1 wt.-%.^{34–36} Our flooding experiment was carried out in an open-system setup, and dissolution/precipitation effects within the pore space were not detected, either by geochemical saturation indices or by microtomography, perhaps due to the relatively short duration of the experiment.

The change in permeability tensor can be explained only by anisotropic mineral dissolution/precipitation and/or particle relocation. The former effect is less likely to have occurred in our sample than the latter. Two phenomena have been suggested in the literature that may induce particle mobility in sandstones. The first has been described as the “water sensitivity of sandstones”,³⁶ such that fluids below a critical salt concentration may cause clay particles to move. In brief, it is induced by van der Waals and electrostatic forces of repulsion between the electric double-layer of clay and quartz interfaces with water. The critical flow rate for remobilization decreases with decreasing salinity of the fluid in the porous media.³⁷ However, the brine used was certainly above this critical salt concentration (Table 1), so the water sensitivity of sandstones cannot explain the migration of clay particles observed in this case. The second phenomenon is simply due to the hydrodynamic force of the fluid and wettability of the particle surface by the fluid. Since both the drag and the interparticle forces determine the deposition rate of fine particles, the interparticle attractive force dominates and the fine particles are deposited rapidly when the flow velocity is sufficiently small. When the flow velocity exceeds a critical value, the drag force dominates and deposition hardly occurs.³⁸ Any change in the flow rate will therefore affect colloid particle movement, but minor precipitate formation on the pore walls not visible at the spatial imaging resolution may also increase the hydrodynamic drag required for colloid detachment.³⁹ Colloidal particles smaller than 1 μ m are also affected by diffusion, while resettling due to filtration occurs where the radius of the particle exceeds the pore opening radius. A minor but constant remobilization/deposition of particles by the mechanisms of interception and

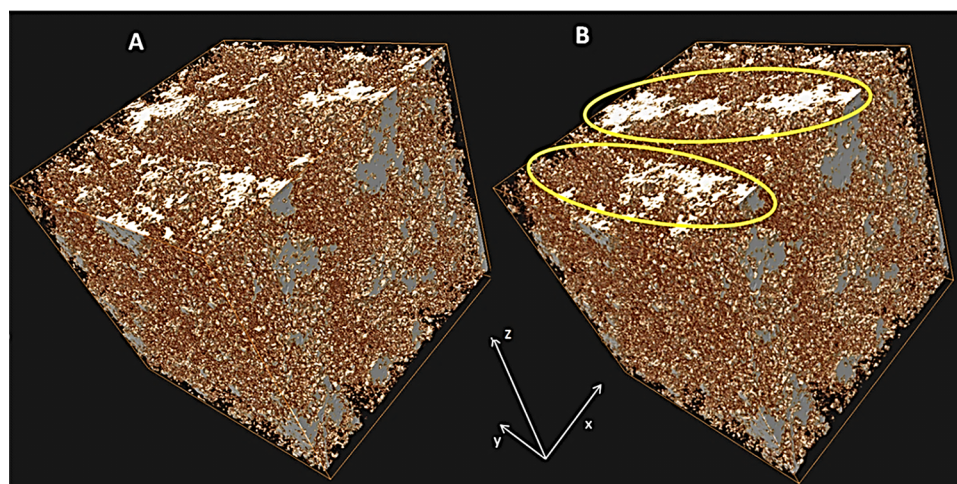


Figure 2. Visualization of the clay mineral assemblages in ROI no. 3 (white and gray areas). (A) shows the pre- and (B) the postflooded state. Areas with visible changes are marked by circles.

filtration may ultimately induce clogging of the pores and thus a significant negative effect on permeability and hydrodynamics even without any significant decrease in overall porosity. This leads to a similar but opposite hydrodynamic effect for minor changes in porosity through a dissolution-induced widening of pore openings.^{6,7,34}

The heterogeneity of the rock sample induces anisotropy in the permeability; a weakly permeable geological stratification of clay mineral assemblages causes higher permeability perpendicular to the z-direction. Although the difference varies with every ROI, due to the heterogeneous distribution of clay minerals in the sample, the effects of and changes in the colloidal mineral distribution along the flow paths must be clearly considered in any predictions of the efficiency of CCS reservoir. Vertical permeability data measured at the Ketzin site are, therefore, clearly underestimating the horizontal flow of the scCO₂, albeit this may change during the sequestration activity.

Postinjection build-up of regions of low permeability in the aquifers can have a strong effect on the efficiency of brine displacement and the residual trapping of scCO₂. It was shown recently by an in situ tomography experiment that the distribution of scCO₂ saturation correlates reasonably well with the distribution of porosity, with higher porosity regions of the rock sample correlating with high residual saturations, and lower porosity regions with lower saturations.^{40–42}

A permeability variation at the microscopic scale can thus induce significant effects on the macroscopic scale. We agree with the authors of these studies that care must be exercised when using average permeability assessments (e.g., using the well-known Berea sandstone reference) to simulate field-scale multiphase flows without consideration of microstructural heterogeneity dynamics and their effect on heterogeneities in scCO₂ saturation.

■ ASSOCIATED CONTENT

■ Supporting Information

Location of the six ROIs within the sample plug (Figure S1), steps in the segmentation routine (Figure S2), error calculation for the segmentation (Table S1), screenshots of the GeoDict code (Figures S3, S4), and steady-state evaluation routine (Figures S5–S7). This material is available free of charge via the Internet at <http://pubs.acs.org>.

■ AUTHOR INFORMATION

Corresponding Author

*Phone: +49 61313924366; fax: +49 61313923070; e-mail: kersten@uni-mainz.de.

Notes

The authors declare no competing financial interest.

■ ACKNOWLEDGMENTS

The authors are grateful for funding and the authorization to publish this work given by Vattenfall AG, Cottbus, Germany. The CO₂SINK project archive provided us with the rock core sample and its characteristics from the Ketzin pilot storage site. Dietmar Meinel and Jürgen Goebbels (BAM Berlin) supplied the μ -XCT data.

■ REFERENCES

(1) Michael, K.; Gloab, A.; Shulakova, V.; Ennis-King, J.; Allinson, G.; Sharma, S.; Aiken, T. Geological storage of CO₂ in saline aquifers - A review of the experience from existing storage operations. *Int. J. Greenhouse Gas Control* **2010**, *4*, 659–667.

(2) Förster, A.; Norden, B.; Zinck-Jørgensen, K.; Frykman, P.; Kulenkampff, J.; Spangenberg, E.; Erzinger, J.; Zimmer, M.; Kopp, J.; Borm, G.; Juhlin, C.; Cosma, C.; Hurter, S. Baseline characterization of the CO₂SINK geological storage site at Ketzin, Germany. *Environ. Geosci.* **2006**, *13*, 145–161.

(3) Prevedel, B.; Wohlgemuth, L.; Legarth, B.; Henningses, J.; Schütt, H.; Schmidt-Hattenberger, C. The CO₂SINK boreholes for geological CO₂ storage testing. *Energy Procedia* **2009**, *1*, 2087–2094.

(4) Würdemann, H.; Möller, F.; Kühn, M.; Heidug, W.; Christensen, N. P.; Borm, G.; Schilling, F. R. CO₂SINK – From site characterization and risk assessment to monitoring and verification: One year of operational experience with the field laboratory for CO₂ storage at Ketzin, Germany. *Int. J. Greenhouse Gas Control* **2010**, *4*, 938–951.

(5) Armitage, P. J.; Faulkner, D. R.; Worden, R. H.; Aplin, A. C.; Butcher, A. R.; Illiffe, J. Experimental measurement of, and controls on, permeability and permeability anisotropy of caprocks from the CO₂ storage project at the Krechba Field, Algeria. *J. Geophys. Res.* **2011**, *116*, B12208 DOI: 10.1029/2011JB008385.

(6) Canal, J.; Delgado, J.; Falcón, I.; Yang, Q.; Juncosa, E.; Barrientos, V. Injection of CO₂-saturated water through a siliceous sandstone plug from the Hontomin test site (N Spain). Experiment and modelling. *Environ. Sci. Technol.* **2012**, DOI: 10.1021/es3012222.

(7) Kempka, T.; Kühn, M.; Class, H.; Frykman, P.; Kopp, A.; Nielsen, C. M.; Probst, P. Modelling of CO₂ arrival time at Ketzin – Part I. *Int. J. Greenhouse Gas Control* **2010**, *4*, 1007–1015.

(8) Förster, A.; Giese, R.; Juhlin, C.; Norden, B.; Springer, N. The Geology of the CO₂SINK Site: From regional to laboratory scale. *Energy Procedia* **2009**, *1*, 2911–2918.

(9) Meyer, R.; May, F.; Müller, C.; Geel, K.; Bernstone, C. Regional search, selection and geological characterization of a large anticlinal structure as a candidate site for CO₂-storage in northern Germany. *Environ. Geol.* **2008**, *54*, 1607–1618.

(10) Zemke, K.; Liebscher, A.; Wandrey, M. CO₂SINK-Group. Petrophysical analysis to investigate the effects of carbon dioxide storage in a subsurface saline aquifer at Ketzin, Germany. *Int. J. Greenhouse Gas Control* **2010**, *4*, 990–999.

(11) Wiese, B.; Böhner, J.; Enachescu, C.; Würdemann, H.; Zimmermann, G. Hydraulic characterization of the Stuttgart formation at the pilot test site for CO₂ storage, Ketzin, Germany. *Int. J. Greenhouse Gas Control* **2010**, *4*, 960–971.

(12) Mahadevan, J.; Sharma, M. M.; Yortsos, Y. C. Flow-through drying of porous media. *AIChE J.* **2006**, *52*, 2367–2380.

(13) Kulenkampff, J.; Spangenberg, E. Physical properties of cores from the Mallik 5L-38 production research well under simulated in situ conditions using the Field Laboratory Experimental Core Analysis System (FLECAS). In *Scientific Results from the Mallik 2002 Gas Hydrate Production Research Well Program, Mackenzie Delta, Northwest Territories*; Dalimore, S. R., Collett, T. S., Eds.; Geological Survey of Canada Bulletin 585 (CD-ROM attachment) : Canada, 2005.

(14) Izgec, O.; Demiral, B.; Bertin, H.; Akin, S. CO₂ injection into saline carbonate aquifer formations I: Laboratory investigation. *Transp. Porous Media* **2008**, *72*, 1–24.

(15) Gallagher, N., Jr.; Wise, G. L. A theoretical analysis of the properties of median filters. *IEEE Trans. ASSP* **1981**, *29*, 1136–1141.

(16) Pal, N. R.; Pal, S. K. A review on image segmentation techniques. *Pattern Recognit* **1993**, *26*, 1277–1294.

(17) Sheppard, A. P.; Sok, R. M.; Averdunk, H. Techniques for image enhancement and segmentation of tomographic images of porous materials. *Phys. A (Amsterdam, Neth.)* **2004**, *339*, 145–151.

(18) Kaestner, A.; Lehmann, E.; Stampanoni, M. Imaging and image processing in porous media research. *Adv. Water Resour.* **2008**, *31*, 1174–1187.

(19) Porter, M. L.; Wildenschild, D. Image analysis algorithms for estimating porous media multiphase flow variables from computed microtomography data: A validation study. *Comput. Geosci.* **2009**, *14*, 15–30.

- (20) Calhoun, P. S.; Duszyk, B. S.; Heath, D. G.; Carley, J. C.; Fishman, E. K. Three-dimensional volume rendering of spiral CT data: Theory and method. *RadioGraphics* **1999**, *19*, 745–764.
- (21) Pfrang, A.; Schladitz, K.; Wiegmann, A.; Schimmel, T. H. Calculation of the evolution of surface area and free volume during the infiltration of fiber felts. *Chem. Vap. Deposition* **2007**, *13*, 705–715.
- (22) Khan, F.; Enzmann, F.; Kersten, M. 3D simulation of the permeability tensor in a soil aggregate on basis of nanotomographic imaging and LBE solver. *J. Soils Sediments* **2012**, *12*, 86–96.
- (23) Bartoli, F.; Bird, N. R. A.; Gomendy, V.; Vivier, H.; Niquet, S. The relation between silty soil structures and their mercury porosimetry curve counterparts: Fractals and percolation. *Eur. J. Soil Sci.* **1999**, *50*, 9–22.
- (24) Fischer, S.; Zemke, K.; Liebscher, A.; Wandrey, M. Petrophysical and petrochemical effects of long-term CO₂ exposure experiments on brine-saturated reservoir sandstone. *Energy Procedia* **2011**, *4*, 4487–4494.
- (25) Pan, C.; Luo, L. S.; Miller, C. T. An evaluation of lattice Boltzmann schemes for porous medium flow simulation. *Comput. Fluids* **2006**, *35*, 898–909.
- (26) Smolarkiewicz, P. K.; Larabee-Winter, C. Pores resolving simulation of Darcy flows. *J. Comput. Phys.* **2010**, *229*, 3121–3133.
- (27) Silin, D.; Tomutsa, L.; Benson, S. M.; Patzek, W. Microtomography and pore-scale modeling of two-phase fluid distribution. *Transp. Porous Media* **2011**, *86*, 495–515.
- (28) Ramstad, T.; Idowu, N.; Nardi, C.; Øren, P.-E. Relative permeability calculations from two-phase flow simulations directly on digital images of porous rocks. *Transp. Porous Media* **2012**, DOI: 10.1007/s11242-011-9877-8).
- (29) Ginzburg, I.; Steiner, K. Lattice Boltzmann model for free-surface flow and its application to filling process in casting. *J. Comput. Phys.* **2003**, *185*, 61–99.
- (30) Ginzburg, I.; d'Humières, D. Multireflection boundary conditions for lattice Boltzmann models. *Phys. Rev. E* **2003**, *68*, 066614.
- (31) d'Humières, D.; Ginzburg, I.; Krafczyk, M.; Lallemand, P.; Luo, L.-S. Multiple-relaxation-time lattice Boltzmann models in three dimensions. *Philos. Trans. R. Soc., A* **2002**, *360*, 437–451.
- (32) Thömmes, G.; Becker, J.; Junk, M.; Vaikuntam, A. K.; Kehrwald, D.; Klar, A. A lattice Boltzmann method for immiscible multiphase flow simulations using the level set method. *J. Comput. Phys.* **2009**, *228*, 1139–1156.
- (33) Izgec, O.; Demiral, B.; Bertin, H.; Akin, S. CO₂ injection into saline carbonate aquifer formations II: Comparison of numerical simulations to experiments. *Transp. Porous Media* **2008**, *73*, 57–74.
- (34) Jové-Colón, C. F.; Oelkers, E. H.; Schott, J. Experimental investigation of the effect of dissolution on sandstone permeability, porosity, and reactive surface area. *Geochim. Cosmochim. Acta* **2004**, *68*, 805–817.
- (35) Giammar, D. E.; Bruant, R. G.; Peters, C. A. Forsterite dissolution and magnesite precipitation at conditions relevant for deep saline aquifer storage and sequestration of carbon dioxide. *Chem. Geol.* **2005**, *217*, 257–276.
- (36) Wigand, M.; Carey, J. W.; Schütt, H.; Spangenberg, E.; Erzinger, J. Geochemical effects of CO₂ sequestration in sandstones under simulated in situ conditions of deep saline aquifers. *Appl. Geochem.* **2008**, *23*, 2735–2745.
- (37) Khilar, K. C.; Fogler, H. S. Water sensitivity in sandstones. *SPE J.* **1983**, *23*, 55–64.
- (38) Hirabayashi, S.; Sato, T.; Mitsuhori, K.; Yamamoto, Y. Microscopic numerical simulations of suspension with particle accumulation in porous media. *Powder Technol.* **2012**, *225*, 143–148.
- (39) Darbha, G. K.; Fischer, C.; Lützenkirchen, J.; Schaefer, T. Site-specific retention of colloids at rough rock surfaces. *Environ. Sci. Technol.* **2012**, DOI: 10.1021/es301969m.
- (40) Ochi, J.; Vernoux, J.-F. Permeability decrease in sandstone reservoirs by fluid injection. Hydrodynamic and chemical effects. *J. Hydrol.* **1998**, *208*, 237–248.
- (41) Perrin, J.-C.; Benson, S. M. An experimental study on the influence of sub-core scale heterogeneities on CO₂ distribution in reservoir rocks. *Transp. Porous Media* **2010**, *82*, 93–109.
- (42) Krevor, S. C. M.; Pini, R.; Zuo, L.; Benson, S. M. Relative permeability and trapping of CO₂ and water in sandstone rocks at reservoir conditions. *Water Resour. Res.* **2012**, *48*, W02532 DOI: 10.1029/2011WR010859.